Ahmed Abdelaziz, Xiaohong Zhang*, Xiaodong Ren, Mostafa Rabah and Ahmed Sedeek*

Impact of temporal resolution in global ionospheric models on satellite positioning during low and high solar activity years of solar cycle 24

https://doi.org/10.1515/jag-2024-0056
Received June 28, 2024; accepted October 17, 2024;
published online November 19, 2024

Abstract: The ionosphere, partially ionized by solar radiation, is rich in free electrons and ions, affecting satellite navigation signals by altering their speed and path. This interaction often leads to signal delays of 5–10 m, complicating accurate positioning in satellite-based systems. This paper investigates the influence of global ionospheric models (GIMs) with varying Temporal Resolutions (TR) on satellite positioning accuracy and convergence time under different solar activities, represented by the years 2009 (low solar activity) and 2014 (high solar activity). The study utilizes Global Positioning System (GPS) data from three GIMs: CODG, representing the Center for Orbit Determination in Europe (CODE) GNSS model with a 2-h TR; bcom, with a 1-h TR; and b5mg, with a 5-min TR. Analysis was conducted using the GNSS Analysis Software for Multi-constellation and Multi-frequency Precise Positioning across 46 international GNSS service stations under single and dual-frequency strategies. The results indicate that precise point positioning convergence time improved by approximately 18 % and 78 % using single and dual frequencies, depending on the GIM applied. Consequently, positioning accuracy after convergence improved by about 16 % and 27 % in the horizontal and up components for ionospheric-constrained single-frequency PPP models and by 68 % and 79 % in the horizontal and up components for dual-frequency PPP models. Furthermore, vertical total electron content analysis at the MARS station revealed significant variations correlating with solar activity, underscoring the importance of selecting appropriate GIMs for accurate GNSS positioning. Future studies, including multi-solar events, are recommended for comprehensive analysis.

Keywords: ionosphere; PPP positioning; high temporal resolution; convergence time; VTEC

***Corresponding authors: Xiaohong Zhang**, The State Key Laboratory of Information Engineering in Surveying, Mapping and Remote Sensing (LIESMARS), Wuhan University, Wuhan, 430079, China; School of Geodesy and Geomatics, Wuhan University, Wuhan 430079, China; Hubei Luojia Laboratory, Wuhan University, Wuhan 430079, Hubei, China; and Chinese Antarctic Center of Surveying and Mapping, Wuhan University, Wuhan 430079, China, E-mail: xhzhang@sgg.whu.edu.cn; and **Ahmed Sedeek**, Department of Mining Engineering, Faculty of Petroleum and Mining Engineering, Suez University, P.O. Box: 43221, Suez, Egypt,
E-mail: Ahmed.Sedeek@pme.suezuni.edu.eg. https://orcid.org/0000-0002-2812-2363
Ahmed Abdelaziz, The State Key Laboratory of Information Engineering in Surveying, Mapping and Remote Sensing (LIESMARS), Wuhan University, Wuhan, 430079, China; and Civil Engineering Department, Benha Faculty of Engineering, Benha University, Benha 13511, Egypt,
E-mail: ahmedes1594@gmail.com
Xiaodong Ren, School of Geodesy and Geomatics, Wuhan University, Wuhan 430079, China; and Hubei Luojia Laboratory, Wuhan University, Wuhan 430079, Hubei, China, E-mail: renxiaodongfly@gmail.com
Mostafa Rabah, Civil Engineering Department, Benha Faculty of Engineering, Benha University, Benha 13511, Egypt,
E-mail: mostafarabah@gmail.com

1 Introduction

The Earth's atmosphere comprises multiple layers, including the ionosphere, which extends from 60 to 1,000 km in altitude. Ionization of the ionosphere is primarily driven by ultraviolet (UV) and X-ray solar radiations, affecting the propagation of GNSS signals as they travel through this ionized layer [1–3]. The refraction of these signals can introduce significant delays, complicating positioning accuracy. Traditionally, GNSS precision position has relied on differential positioning, which requires measurements from multiple receivers [4]. While effective, this method is limited by the need for a reference receiver. Precise Point Positioning (PPP) allows positioning using a single receiver by modelling and correcting all GNSS errors and biases. A common approach in PPP is using ionosphere-free combinations of code and carrier-phase data to eliminate first-order ionospheric effects. This linear combination, on the other hand, results in a residual ionospheric delay component of up to a few centimetres, which represents higher-order ionospheric terms [5–7].

Satellite orbit and clock errors are adjusted utilizing precise products from the International GNSS Service (IGS) [8]. Receiver clock errors can also be estimated, while other

factors like ocean loading, Earth tides [9], carrier-phase windup [10], relativity, and antenna phase-center variations can be modelled and corrected with high accuracy [11]. Empirical models (e.g., Saastamoinen or Hopfield models) or tropospheric corrections generated from regional GPS networks, such as the National Oceanic and Atmospheric Administration (NOAA) tropospheric corrections, can be used to account for tropospheric delay (NOAATrop) [11, 12]. Currently, the IGS exact orbit and clock products do not consider the second-order ionospheric delays, which can degrade the PPP accuracy. Therefore, correcting higher-order ionospheric delays is critical for improving PPP performance [13, 14]. While smaller than first-order effects, these higher-order terms still contribute to positioning errors, particularly during periods of increased solar activity and geomagnetic disturbances [15, 16].

Until 2014, all Global Ionospheric Maps (GIMs) had a 2-h temporal resolution (TR). In 2015, some international associate analysis centers (IAACs) started to offer higher resolution products (30–60 min), allowing for more detailed ionospheric modelling. Recent studies, such as those by Wang [16], have evaluated GIMs using PPP and found that certain GIM products, such as CODG, ESAG, WHUG, and CASG, underestimate vertical total electron content (VTEC) during periods of high solar activity, particularly over the equatorial ionization anomaly (EIA).

Gabriel et al. [17] assessed GIM using ionosonde data. The study analyzed one year of data from 2015, evaluating thirteen GIMs, with CODG and UQRG showing the best performance. A four-year time series (2014–2017) focused on these two models revealed regional and temporal ionospheric variations, particularly larger errors during the solar cycle peak in 2014 and in areas with widely spaced ionosondes. The findings confirm the effectiveness of the developed method for assessing GIM quality using ionosonde data. Additionally, Gabriel et al. [18] introduced a clear understanding of the benefits of using regional ionospheric maps (RIMs) over GIMs. GNSS positioning resulted in more significant, noisier errors near the equatorial anomaly. Two of the studied RIMs showed significant errors in stations on the margins of the coverage area.

This study evaluates two newer GIMs, b5mg (5-min resolution) and bcom (60-min resolution), by comparing their impact on positioning accuracy and convergence time against the widely used CODG GIM. Focusing on undifferenced and uncombined observation data from multiple GNSS stations across Western Europe, the study investigates how ionospheric conditions influence GNSS positioning during years of low and high solar activity (2009 and 2014) in solar cycle 24 by applying single and dual frequency. The study investigates how temporal variations of GIMs influence satellite positioning accuracy and convergence time under different solar activity levels. Based on the ionospheric and geomagnetic activities observed on DOY 079, 173, 266, and 356 of 2009 and 2014 – representing the equinoxes and solstices during years of low and high solar activity, respectively [19] – we calculate the VTEC and analyze its correlation with positioning accuracy and convergence performance.

The data section will provide an overview of the data sources and study period. Section 3 will outline the methodology, followed by the presentation and discussion of results in Section 4. Finally, the conclusions will be summarized in Section 5.

2 Datasets

Solar cycles span roughly 11 years, alternating between maximum and minimum sunspot activity periods. Solar Cycle 24, the most recent complete cycle, which began in December 2008, reached a smoothed sunspot minimum of 2.2 and concluded in December 2019. Solar activity was minimal until early 2010, peaking in April 2014 with a sunspot number of 81.8. This peak was notably weaker than previous cycles, reaching levels not seen since the late 19th and early 20th centuries [20, 21]. While solar activity in 2009 remained low, 2014 showed a significant surge, as evidenced by the solar flux (f10.7) data presented in Figure 1, which compares 2009 (blue) and 2014 (red).

The Kp-index is a global metric for geomagnetic activity derived from 3-hourly measurements taken by ground-based magnetometers worldwide. Each station computes a local Kp-index based on geomagnetic disturbances relative to a quiet day baseline. The global Kp-index, ranges from 0 (minimal activity) to 9 (severe geomagnetic storms) and is computed by combining local values. 2009, the Kp-index remained low due to reduced solar flare activity (Figure 2). In contrast, 2014 witnessed higher Kp-index levels (Figure 3), reflecting increased solar and geomagnetic activity. The comparison of Kp-index values during the equinoxes and solstices of 2009 and 2014 clearly highlights 2009 as a year of low solar activity and 2014 as one of high activity – an ideal contrast for this study.

Global Ionospheric Maps typically offer TRs of one to 2 h, limiting their precision in detailed ionospheric studies. However, recent advancements, such as the 30-s resolution GIMs from Beihang University STAR Lab, offer valuable insights for studying ionospheric weather and climatology, although these are still experimental. This study evaluates the influence of high-TR GIMs, particularly the 5-min (b5mg)

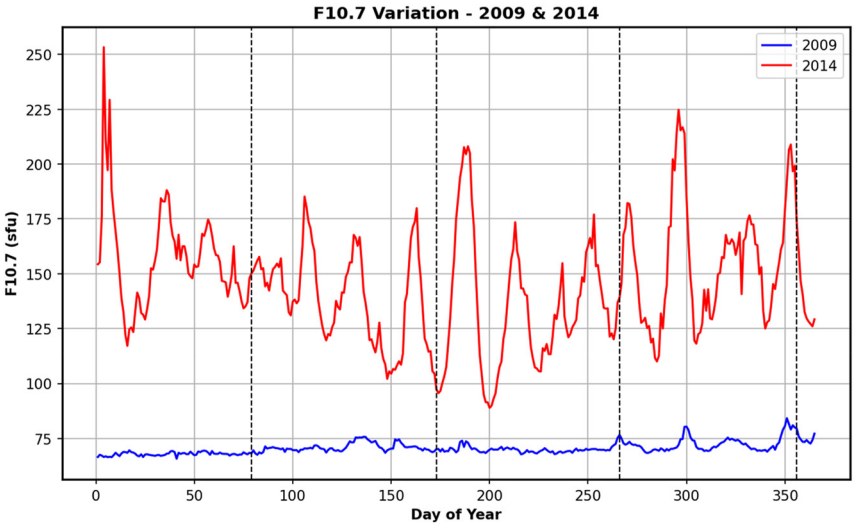

Figure 1: Shows the solar flux (f10.7) for the years 2009 (blue line) and 2014 (red line), as sourced from OmniWeb (https://omniweb.gsfc.nasa.gov/), with 4 black dotted lines at DOYs 79, 173, 266, and 356.

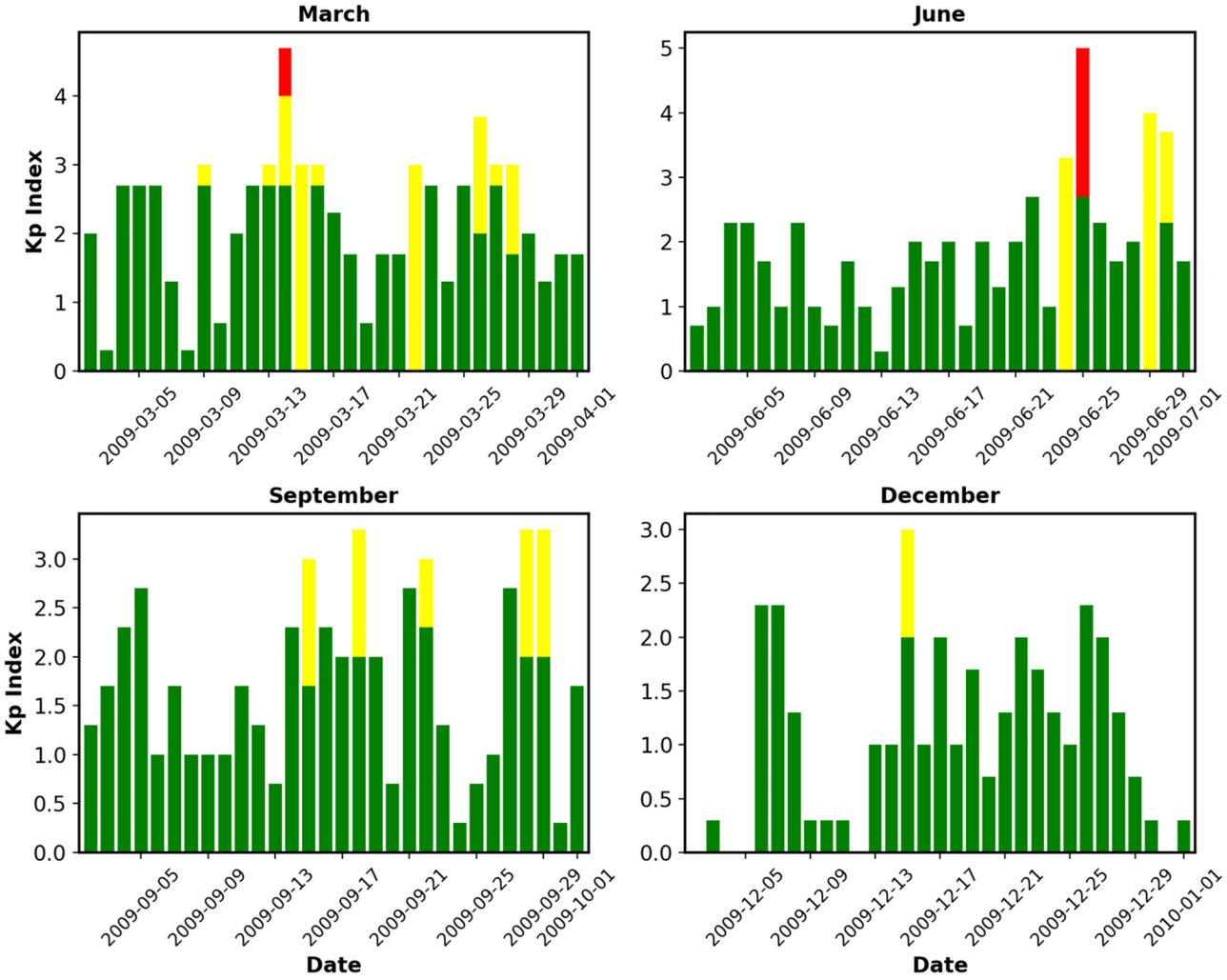

Figure 2: Illustrates the Kp-index throughout 2009, covering the equinoxes (March and September) and solstices (June and December), based on data sourced from OmniWeb (https://omniweb.gsfc.nasa.gov/).

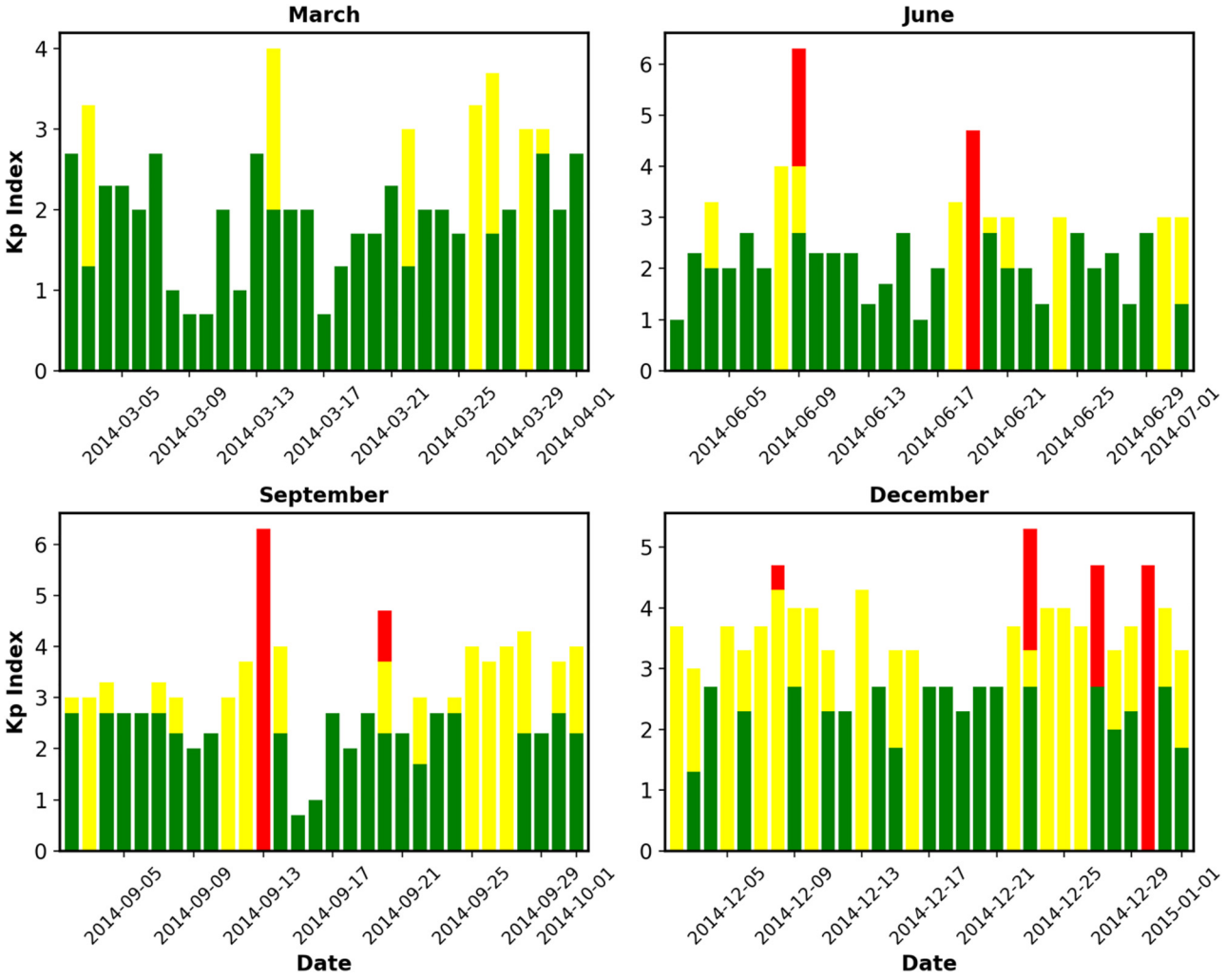

Figure 3: Illustrates the Kp-index throughout 2014, covering the equinoxes (March and September) and solstices (June and December), based on data sourced from OmniWeb (https://omniweb.gsfc.nasa.gov/).

and 60-min (bcom) GIMs, on the accuracy of GNSS positioning during ionospheric disturbances.

Stations in Western Europe were selected due to the high density of available data, which enabled a robust analysis using three IONEX GIMs: CODG, bcom, and b5mg (Figure 4). The study covers 46 stations and focuses on data from 2009 to 2014, representing periods of low and high solar activity, respectively. Seasonal variations were examined through undifferenced and uncombined observations during the March Equinox, June Solstice, September Equinox, and December Solstice. These were evaluated using IONEX files with TRs of 120, 60, and 5 min to assess the performance of higher resolution GIMs. The study primarily focused on mid-latitude stations, with latitudes between 20° and 60°.

3 Methodology

This study analyzes GNSS data from 46 stations using different estimation strategies for single-frequency (SF) and dual-frequency (DF) processing, as summarized in Table 1. The primary distinction between SF and DF processing lies in the number of frequencies used: SF processes data from one frequency, while DF utilizes two. The “Ionoopt” parameter highlights this difference, with SF applying ionospheric corrections based solely on the single frequency (UC1), whereas DF processing computes more precise correction by leveraging both frequencies (UC12). The table also highlights that both processing modes employ a GPS navigation system, float ambiguity resolution, and a kinematic PPP positioning mode, with a cut-off elevation angle set to 10°.

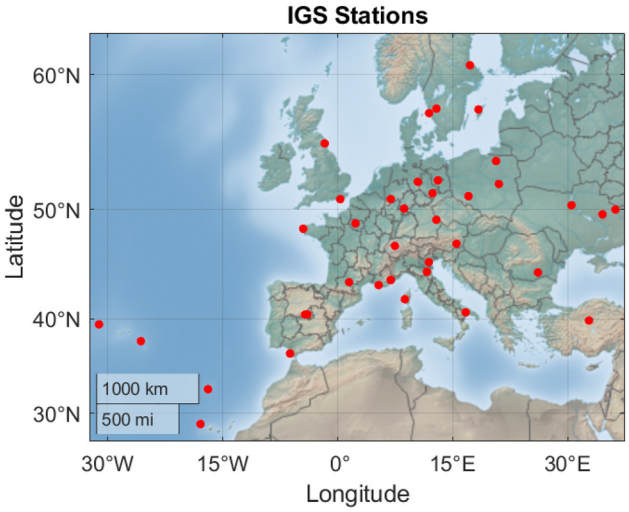

Figure 4: Illustrates the cluster of IGS stations across western Europe, represented by red dots.

Table 1: Parameters and estimation strategies for single and dual-frequency processing.

Parameter	Single frequency (SF)	Dual frequency (DF)
Navsys	GPS	
Ambiguity	Float ambiguities	
Posmode	ppp_kinematic	
Cut-off elevation (deg)	10	
Processing frequencies	1	2
Ionoopt	UC1: ionospheric corrections based on single-frequency data.	UC12: utilize both frequencies for a more precise correction

The methodology is further outlined in the flowchart (Figure 5), which details the steps to analyze GNSS data under varying solar activity conditions, utilizing the GAMP (GNSS Analysis software for Multi-constellation and multi-frequency Precise positioning) software. The process begins by categorizing data based on solar activity levels – distinguishing between low and high solar activity periods. GNSS observation data, stored in the RINEX format and precise Ephemeris data, are processed in GAMP. Key outputs from this analysis include PPP convergence times, positioning accuracy, and Slant Total Electron Content (STEC) calculations. Then, ionospheric corrections are applied using IONEX files derived from three GIMs: CODG, bcom, and b5mg. These outputs are then further analyzed and visualized using Matlab, enabling a detailed assessment of positioning accuracy and the effect of ionospheric conditions across different levels of solar activity.

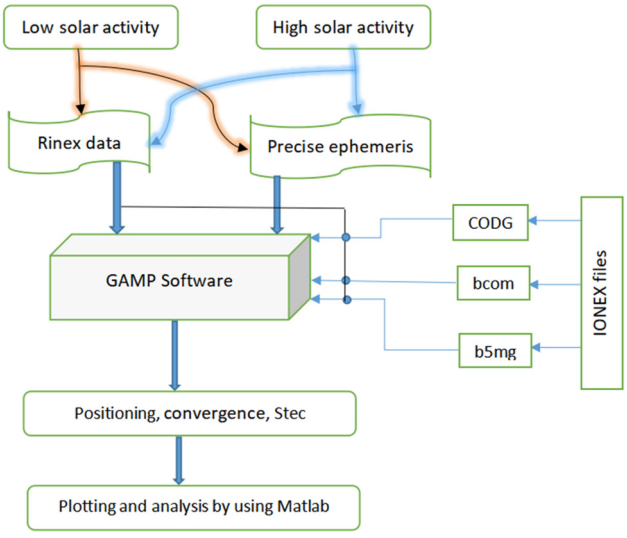

Figure 5: Flowchart illustrating the procedures followed in the processes.

For the L_k frequency ($k = 1$ or 2), the observation formulas for code and carrier phase measurements can be expressed according to Ren [22] as follows:

$$\begin{cases} P_{k,r}^{s} = \rho_{0,r}^{s} + d_{ion,k,r}^{s} + d_{trop,r}^{s} + c(\tau_r - \tau^s) + d_k^s - d_{k,r} + \varepsilon_{p,k,r}^{s} \\ L_{k,r}^{s} = \rho_{0,r}^{s} - d_{ion,k,r}^{s} + d_{trop,r}^{s} + c(\tau_r - \tau^s) + \lambda N_k^s + b_k^s - b_{k,r} + \varepsilon_{L,k,r}^{s} \end{cases} \tag{3.1}$$

where s is the satellite; r is the receiver; k denotes frequency; ρ_0 is the satellite-to-receiver range; P represents the pseudo-range observation; L represents the carrier phase observation; d_{ion} stands for ionospheric delay error; d_{trop} is the tropospheric delay error; τ_r denotes the receiver clock error; τ^s is the satellite clock error; d represents the differential code bias; b represents the differential phase bias; N_k^s represents the initial integer ambiguity; ε_p and ε_L Represent the pseudo-range and phase observation noise, respectively, incorporating errors such as multi-path effects and satellite orbit errors.

Precise satellite orbit and clock products the IGS provides are typically employed for PPP procedures [23]. Because precise satellite orbits and clocks are derived using an ionosphere-free combination of both code and phase measurements, the hardware delays associated with code measurements for both L1 (1,575.42 MHz) and L2 (1,227.60 MHz) frequencies that are used for GPS satellites are accounted for within the satellite clock offset [24].

The equation below expresses how the clock offset incorporates the impact of these dual-frequency signals:

$$\tilde{t}^s = t^s - \frac{\mu_k}{\mu_k - 1} d_1^s + \frac{1}{\mu_k - 1} d_2^s \tag{3.2}$$

In this equation, d_1^s and d_2^s represent the hardware delays for the L1 and L2 frequencies, respectively, and $\mu_k = \frac{f_1^2}{f_k^2}$, where f_1 for L1 and f_k for the L1 and L2 frequencies. The parameter μ_k scales the relationship between these frequencies, highlighting the ionospheric-free nature of the combination. The equation demonstrates how the clock corrections incorporate the frequency-dependent biases and delays in the dual-frequency GPS signals, ensuring more accurate PPP positioning. The study derives the full-rank linearized observation equation for PPP by incorporating Equation (3.2) into Equation (3.1), as demonstrated in Equation (3.3) [25].

$$\begin{cases} \Delta P_{r,k}^s = -\gamma_r^s \cdot x_r + \bar{t}_r + M_{w,r}^s T_{w,r} + \mu_k \tilde{I}_{r,1}^s \\ \Delta L_{r,k}^s = -\gamma_r^s \cdot x_r + \bar{t}_r + M_{w,r}^s T_{w,r} - \mu_k \tilde{I}_{r,1}^s + \overline{N}_{r,k}^s \end{cases} \tag{3.3}$$

where $\Delta P_{r,k}^s$ and $\Delta L_{r,k}^s$ are the observed minus calculated (OMC) observations necessary to correct all systematic errors mentioned earlier; γ_r^s is the unit vector from the receiver to satellite antennas; x_r is the correction to the approximate coordinates of the receiver; $\bar{t}_r$ is the estimated receiver clock offset; $T_{w,r}$ and $M_{w,r}^s$ denote the zenith wet tropospheric delay and its corresponding mapping function that is used to transform zenith wet tropospheric delay to slant wet tropospheric delay; $\tilde{I}_{r,1}^s$ denotes the ionospheric observable to be estimated; μ_k is the frequency-dependent multiple factor; $\overline{N}_{r,k}^s$ is the ambiguity parameter including the frequency-dependent receiver and satellite uncalibrated phase delays (UPDs). The ionosphere-constrained SF PPP incorporates virtual observations of ionospheric parameters and limitations into the observation equations, as Zhou et al. Introduced [26], assuming the receiver r simultaneously tracks m satellites.

$$\begin{bmatrix} \Delta P_{r,1}^{1,s} \\ \Delta L_{r,1}^{1,s} \\ \vdots \\ \Delta P_{r,1}^{m,s} \\ \Delta L_{r,1}^{m,s} \\ \tilde{I}_{r,1}^{1,s} \\ \vdots \\ \tilde{I}_{r,1}^{m,s} \end{bmatrix} = \begin{bmatrix} -u_r & 1 & M_w & K & R_1 \\ 0 & 0 & 0 & I & 0 \end{bmatrix} \begin{bmatrix} x_r \\ \bar{t}_r \\ T_{w,r} \\ I_{r,1}^s \\ \overline{N}_{r,1}^s \end{bmatrix} + \begin{bmatrix} \varepsilon_{p,r,1}^s \\ \varepsilon_{L,r,1}^s \\ \varepsilon_{r,ion}^s \end{bmatrix}, Q_L, Q_I \tag{3.4}$$

where 1 is a vector of $2 \times m$ rows and one column, of which each element is one, corresponding to the receiver clock parameter $\bar{t}_r$; in matrix K, the element for the corresponding $\Delta P_{r,k}^s$ is 1, while the element for $\Delta L_{r,k}^s$ is −1, corresponding to the ionospheric parameter $I_{r,1}^s$ with corresponding noise $\varepsilon_{r,ion}^s$; R_1 is the matrix corresponding to the ambiguity parameters $\overline{N}_{r,1}^s$; where the element for the corresponding $\Delta P_{r,k}^s$ is 0, while for $\Delta L_{r,k}^s$ is 1; $^- Q_L$ denotes the stochastic model of OMC observables; Q_I denotes the stochastic model of virtual ionospheric observables; 0 is zero matrix; I is the identity matrix. Additionally, The ionosphere-constrained DF PPP incorporates virtual observations of ionospheric parameters and limitations into the observation equations with R_2 as the matrix corresponding to the ambiguity parameters $\overline{N}_{r,2}^s$, as shown in equation (3.5), and the element for the corresponding $\Delta P_{r,k}^s$ is 0, while for $\Delta L_{r,k}^s$ is 1. For more details, one can refer to [26].

$$\begin{bmatrix} \Delta P_{r,1}^{1,s} \\ \Delta L_{r,1}^{1,s} \\ \vdots \\ \Delta P_{r,2}^{m,s} \\ \Delta L_{r,2}^{m,s} \\ \tilde{I}_{r,1}^{1,s} \\ \vdots \\ \tilde{I}_{r,1}^{m,s} \end{bmatrix} = \begin{bmatrix} -u_r & 1 & J & M_w & K & R_1 & R_2 \\ 0 & 0 & 0 & 0 & I & 0 & 0 \end{bmatrix} \times \begin{bmatrix} x_r \\ \bar{t}_r \\ DCB_{r,p_1,p_2} \\ T_{w,r} \\ I_{r,1}^s \\ \overline{N}_{r,1}^s \\ \overline{N}_{r,2}^s \end{bmatrix} + \begin{bmatrix} \varepsilon_{p,r,1}^s \\ \varepsilon_{L,r,1}^s \\ \varepsilon_{r,ion}^s \end{bmatrix}, Q_L, Q_I \tag{3.5}$$

where DCB_{r,p_1,p_2} is frequency-dependent receiver DCB between the two pseudoranges P_1 and P_2; I is the identity matrix; for matrix J the element for the corresponding $\Delta P_{r,1}^{m,s}$ is $\left(\frac{1}{\mu_k - 1}\right)$, while the element for $\Delta P_{r,2}^{m,s}$ is $-\left(\frac{\mu_k}{\mu_k - 1}\right)$, corresponding to the receiver DCB. In this study, the ionospheric observable was utilized for TEC retrieval and can be represented as follows:

$$\begin{cases} \tilde{I}_{r,1}^s = I_{r,1}^s - \dfrac{1}{\mu_k - 1}\left(d_{12}^s + d_{r,12}\right) \\ d_{12}^s = d_1^s - d_2^s; \quad d_{r,12} = d_{r,1} - d_{r,2} \end{cases} \tag{3.6}$$

where d_{12}^s and $d_{r,12}$ represent satellite and receiver differential code biases, respectively [26], considering that the

$d_{r,12} \equiv \mathrm{DCB}_{r,p_1,p_2}$, representing the receiver differential code bias between pseudoranges $\Delta P^{1,s}_{r,1}$ and $\Delta P^{m,s}_{r,2}$.

Ionospheric VTEC is a metric that quantifies the number of electrons traveling across a unit area and is denominated in TECU. One TECU equals 10^{16} electrons per square meter. In the context of GNSS signal propagation, it is assumed that all electrons along the signal's propagation path are concentrated in an idealized thin layer of minimal thickness. This thin layer is thought to be located at an elevation of 450 km. The Slant Total Electronic Content (STEC) along the slant propagation path is estimated using single-site DF observational data. STEC is then turned into VTEC using a projection mapping function [27].

Using a single-layer model projection function, the STEC is ultimately transformed into the VTEC above the measurement station. The process is as follows:

$$\begin{cases} \mathrm{VTEC}^s_r = M(Z^s_r) \cdot \left(\dfrac{f_1^2}{c} \tilde{I}^s_{r,1} + \dfrac{f_1^2}{c(\mu_k - 1)} \left(d^s_{12} + d_{r,12} \right) \right) \\ M(Z^s_r) = \left(1 - \dfrac{\sin^2(Z^s_r)}{\left(1 + \frac{H}{R_e}\right)} \right) \end{cases} \tag{3.7}$$

In this context, $M(Z^s_r)$ represents the mapping function used to convert slant TEC into VTEC, where Z^s_r is the satellite's zenith distance, and H represents the altitude of the ionospheric thin-layer shell taken as 450 km, with 6,371 km as the radius of the Earth (R_e); c is a constant with a value of 40.28×10^{16} m s^{-2} TECU^{-1}.

4 Result and discussion

4.1 Impact of high temporal resolution GIMs and solar activity on convergence time

PPP convergence is where position estimates or float ambiguities stabilize at specific accuracy levels without significant deviation. Several factors influence convergence time, including satellite geometry, receiver environment and dynamics, and observation intervals and assurance. During low solar activity, the convergence time using SF signals was approximately 586 min, longer than the 477 min observed during high solar activity (Figure 6a and c). Notably, convergence time improved by 18.46 % during the March equinox

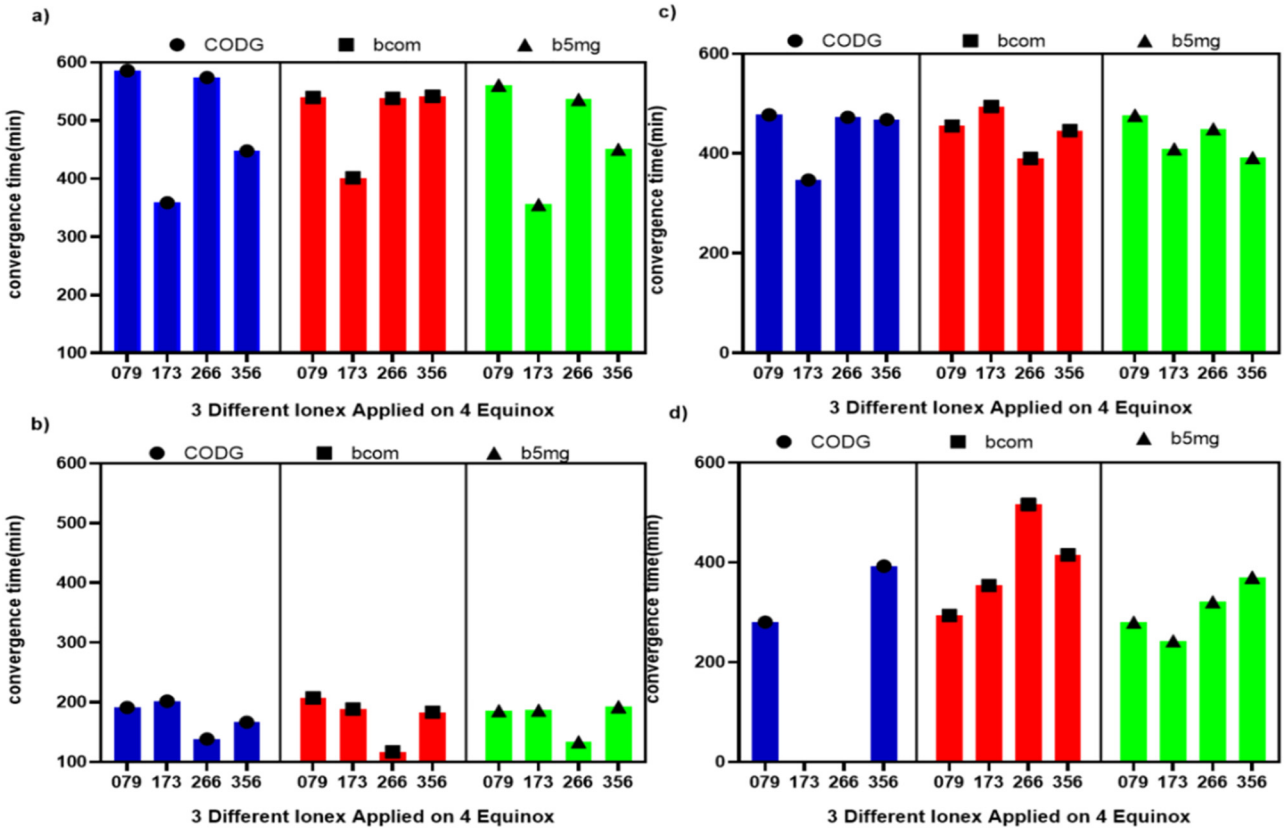

Figure 6: Average convergence time of PPP processing during low and high solar activity using single and dual frequency across three different IONEX files for four equinoxes: (a) S-F, 2009; (b) D-F, 2009; (c) S-F, 2014; (d) D-F, 2014.

Table 2: Average convergence time of PPP processing for low and high solar activity using SF and DF through three different IONEX files during four equinoxes.

Solar activity periods	IONEX files	Average convergence time (min) through four equinoxes			
		79	173	266	356
2009, S.F	CODE	585.97	358.84	574.22	447.96
	bcom	539.76	401.55	538.27	542.04
	b5mg	560.9	355.94	536.74	450.68
2009, D.F	CODE	191.28	202	138.43	166.76
	bcom	207.28	188.72	116.72	183.51
	b5mg	186.14	187.08	133.88	192.43
2014, S.F	CODE	477.79	347.26	472.89	468.35
	bcom	455.19	494.58	390.46	446.11
	b5mg	476.75	409.66	449.54	392.01
2014, D.F	CODE	280.49	–	–	392.65
	bcom	293.8	353.84	516.15	415.39
	b5mg	280.49	242.92	321.35	370.29

using the CODG IONEX file, with a smaller 3.23 % improvement during the June equinox. However, 2014, convergence times were significantly longer than in 2009, particularly during the June equinox using the bcom and b5mg IONEX files (Table 2).

When using DF signals, convergence times in 2014 were generally longer than in 2009 (Figure 6b and d). Unlike SF, DF observations showed no significant difference between low and high solar activity periods (Figure 6c and d). In contrast, DF signals significantly improved convergence time compared to SF signals during 2009. For instance, using the CODG IONEX file, DF signals led to a 43.71 %–75.89 % improvement across the equinoxes, with the most significant improvement during the September equinox as in blue panels. Similar improvements were seen with the bcom IONEX file, ranging from 53 % to 78.32 % across the equinoxes.

2014 DF signals notably improved, albeit less than during low solar activity periods. For instance, the b5mg IONEX file showed improvements between 5.54 % and 41.17 % across the equinoxes. These findings suggest that DF was more effective in 2009 than 2014, contrary to SF observations. Furthermore, solar activity influenced the higher TR model (b5mg) more than the CODG and bcom models employing DF versus SF in 2014. These findings align with studies by Liu [10] and Wu [28], who found similar trends in PPP convergence times.

In conclusion, PPP convergence times significantly improve from single-to dual-frequency during low solar activity. However, during high solar activity, results vary, with some improvements and occasional worsening. These variations may be attributed to the limited accuracy of GIMs, which have a vertical precision of 2–8 TECU [29], leading to a GPS L1 frequency signal range inaccuracy of 0.32–1.28 m. The high TR model (b5mg) outperformed low TR models (CODG and bcom) during periods of high solar activity.

4.2 Impact of high temporal resolution GIMs on positioning accuracy post-convergence

The improvements in convergence time observed during 2009, as previously discussed, had a significant impact on positioning accuracy. Figures 7 and 8 illustrate the differences in positioning accuracy before and after convergence for both SF and DF. Positioning accuracy improved by 16 % and 27 % in the horizontal and vertical components, respectively, using ionospheric-constrained SF in the left column through Figure 7. In contrast, DF signals saw more substantial improvements of 68 % and 79 % in the same components, as shown in the left column from Figure 8. During 2014, positioning accuracy improved as well, with enhancements of 22 % and 13 % in the horizontal and vertical components for SF, as in the right column from Figure 7, and 54.27 % and 45.66 % for DF signals, as in the right column of Figure 8.

For further clarity, during periods of low solar activity in the March equinox, SF signals improved horizontal accuracy by 33 %, 28 %, and 34 % using CODG, bcom, and b5mg IONEX files, respectively. The corresponding improvements in the vertical component were 13 %, 18 %, and 20 %. However, the vertical component witnessed greater improvements for the other equinoxes than the horizontal component. For example, in the September equinox, vertical accuracy improved by 28 %, 30 %, and 23 % for CODG, bcom, and b5mg, respectively, while the horizontal showed no

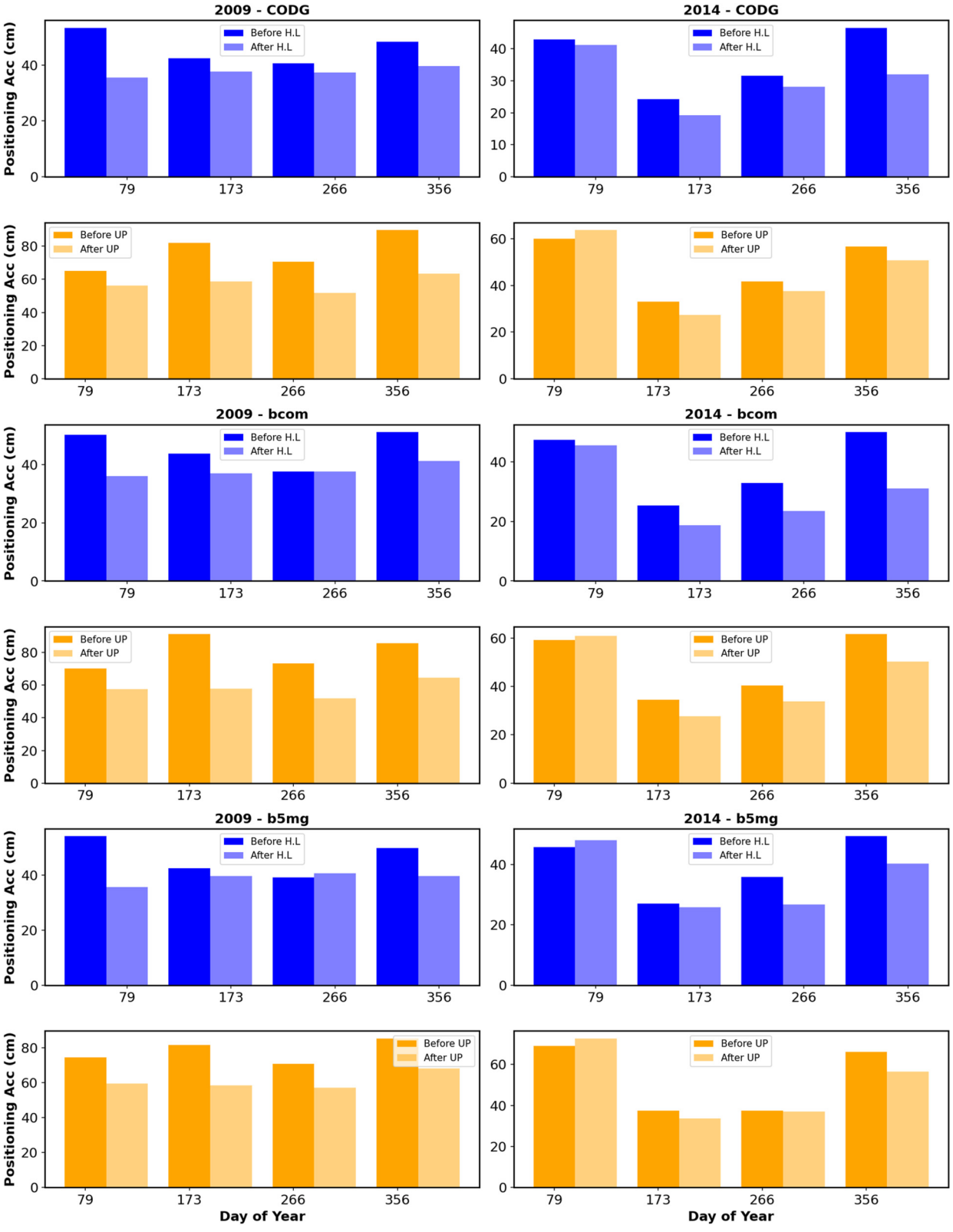

Figure 7: Average positioning accuracy (cm) in H.L and UP components before and after convergence using CODG, bcom, and b5mg IONEX files with single frequency. The blue bars represent the H.L component, and the orange bars represent the UP component, the same for next figure.

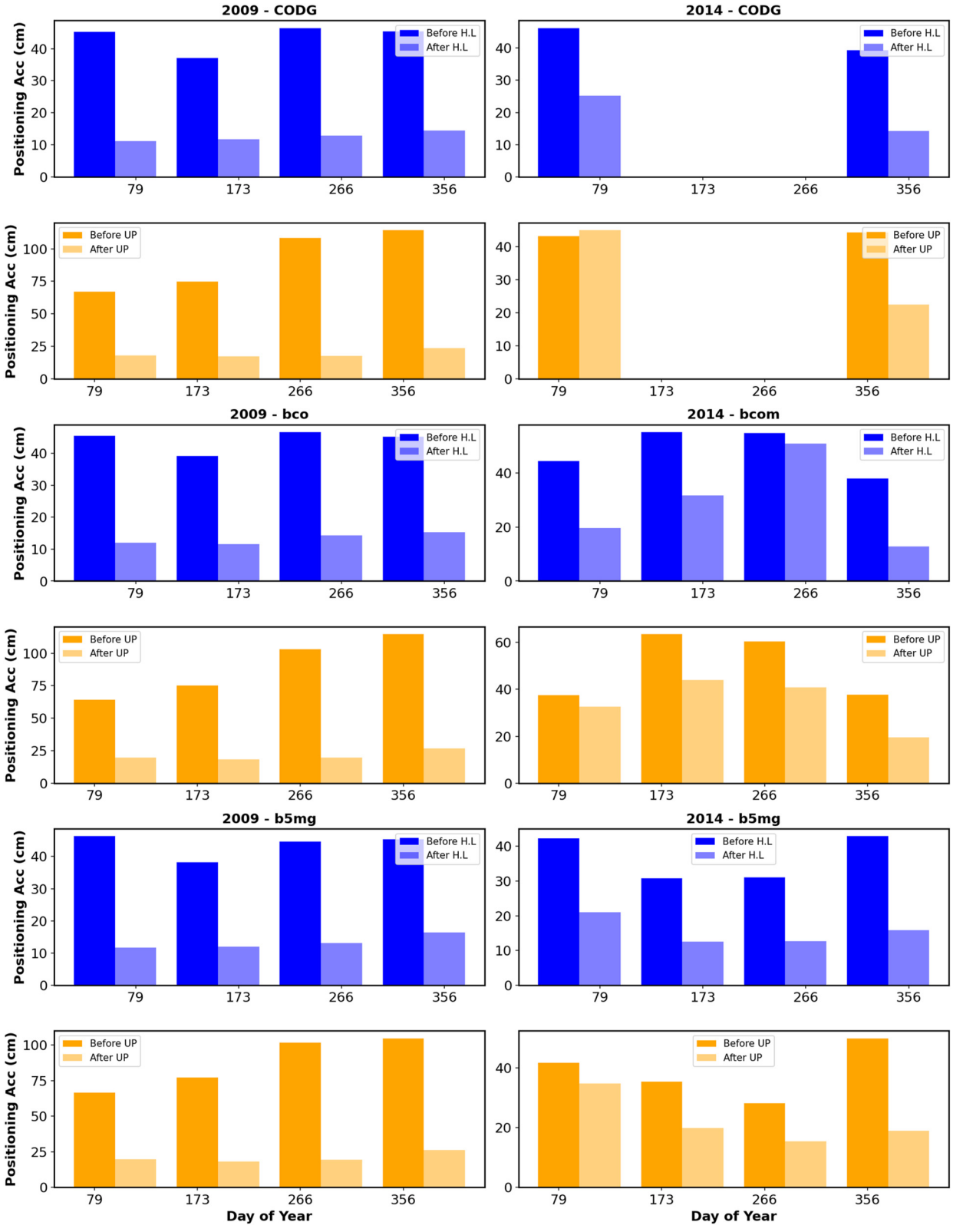

Figure 8: Average positioning accuracy (cm) in horizontal and vertical components before and after convergence using CODG, b5mg, and bcom IONEX files with dual frequency.

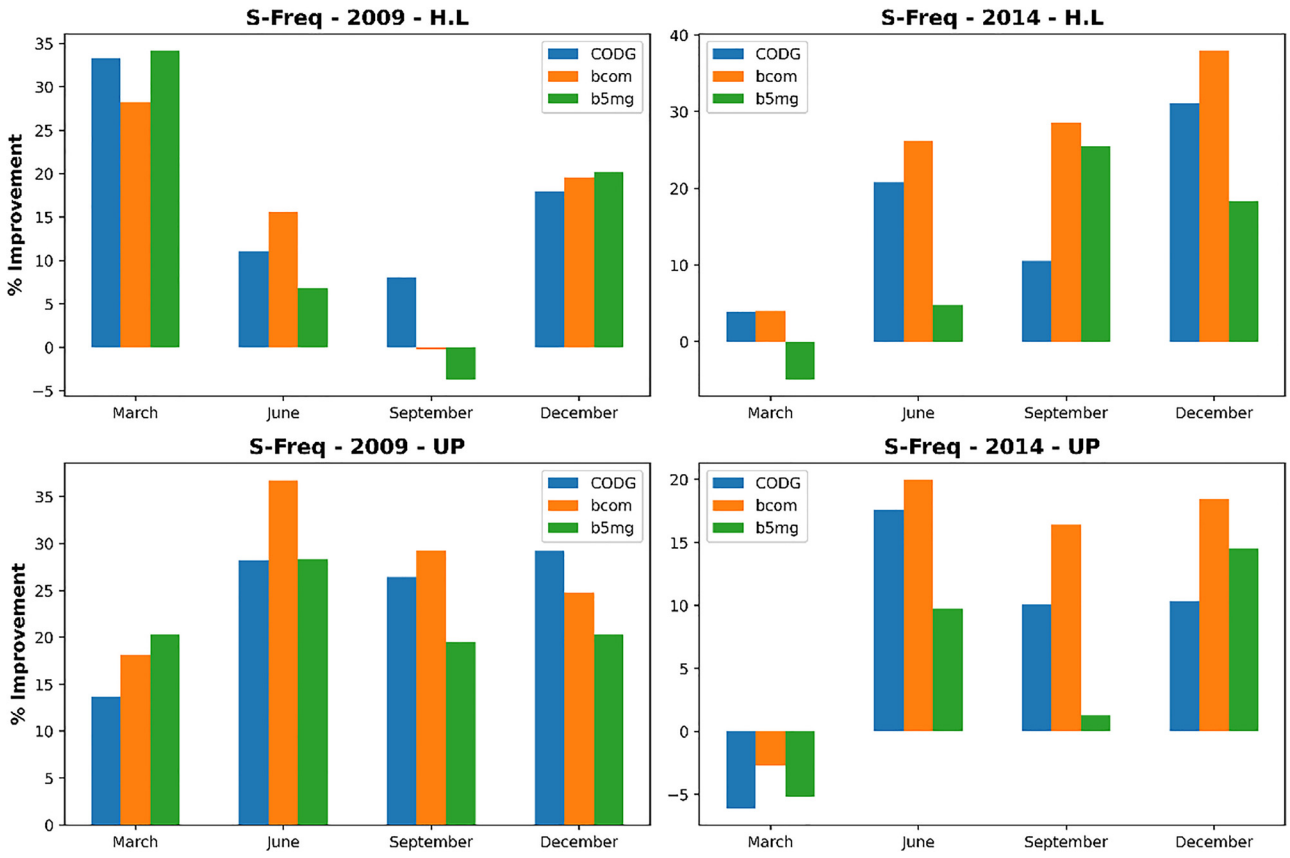

Figure 9: Percentage improvement in positioning accuracy after convergence time for CODG, bcom, and b5mg during high and low solar activity periods, using sual frequency.

improvement with bcom and b5mg and only 8 % with CODG (Figure 9). There was also a slight decline in the horizontal component during the June equinox and an increase during the December equinox.

In high solar activity years, using SF negatively affected the vertical component for all three IONEX files during the March equinox. The horizontal component, However, improved with CODG and bcom files. In the June, September, and December equinoxes, the horizontal component improved by 21 %, 11 %, and 31 % for CODG IONEX, and 26.2 %, 28.6 %, and 38 % for bcom IONEX. The vertical component also showed improvements, though to a lesser extent. During low solar activity periods, DF signals pronounced improvements, particularly in the March equinox, with horizontal component improving by about 75 %, 73 %, and 73.7 % using CODG, bcom, and b5mg IONEX files, respectively (Figure 10). The vertical component also improved but to a slightly lesser extent. The improvements in the other equinoxes were significant in both components, particularly in the horizontal.

The horizontal component generally improved more during high solar activity than the vertical component. There was no improvement in the vertical component for the March equinox, while the horizontal component improved by about 45 % using CODG Ionex file. The horizontal and vertical components improved by approximately 64 % and 49 % during the December solstice. For the bcom and b5mg IONEX files, improvements in the horizontal component varied across the equinoxes, with the most significant improvements in the December solstice. The vertical component showed lower levels of improvement compared to the horizontal. Contrary to recent studies by Liu [10], which demonstrated that the accuracy of GIMs with a time resolution of 60 min or less is consistent, our findings indicate that a 5-min TR offers significantly better accuracy than a 60-min resolution. This suggests that further investigation is needed into the impact of high TR GIMs on PPP positioning accuracy.

The VTEC data for 2009 and 2014 at the MARS station (Lat: 43.279°, Lon: 5.354°) underscore the significant impact of solar activity on ionospheric conditions and GNSS performance. The comparison between SF and DF PPP models demonstrates the superiority of DF systems in mitigating ionospheric errors, particularly during periods of

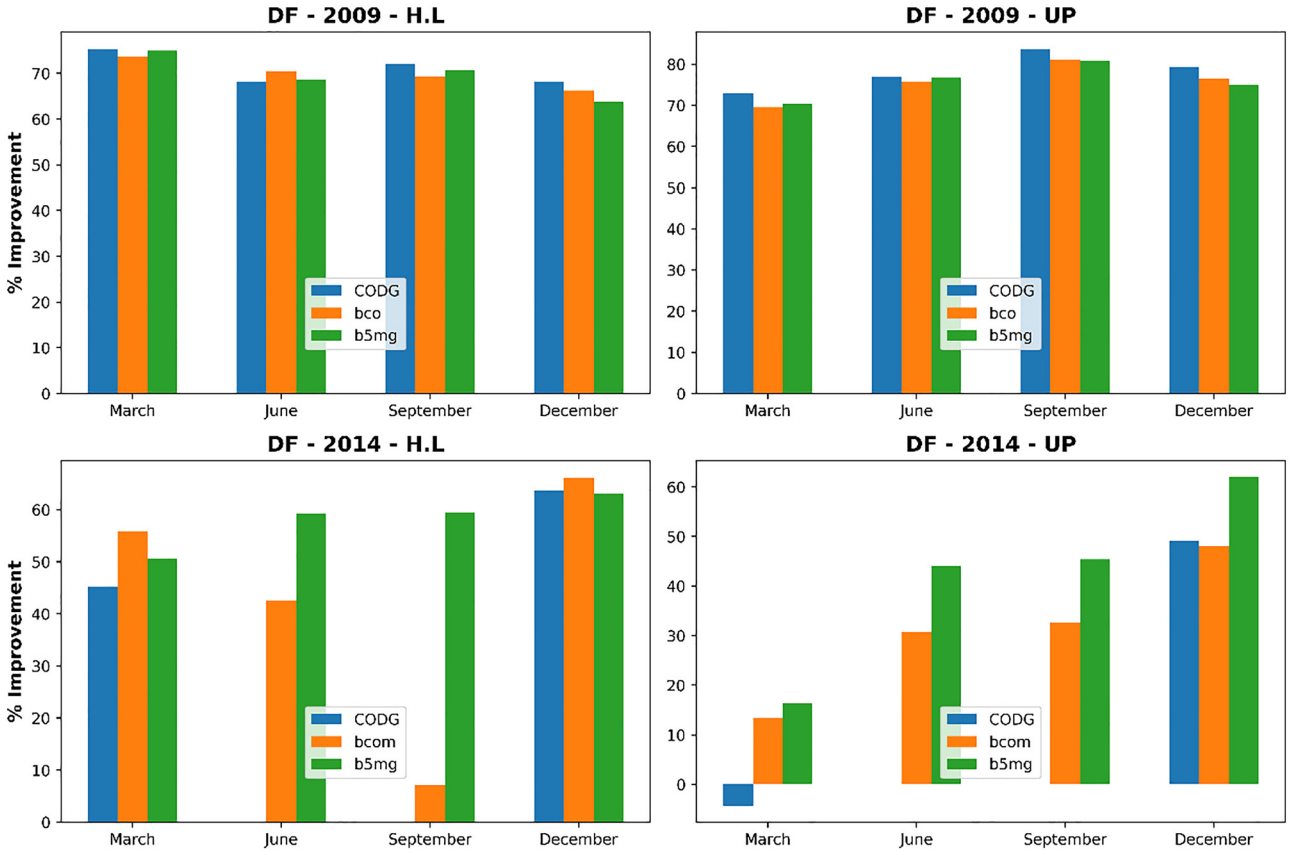

Figure 10: Percentage improvement in positioning accuracy after convergence time for CODG, bcom, and b5mg during high and low solar activity periods, using dual frequency.

heightened solar activity, corroborating existing research in this area. Figures 11 and 12 illustrate the VTEC obtained from the three IONEX files (CODG, bcom, and b5mg). These figures contrast the temporal distribution of VTEC in SF and DF configurations. The data reveals a notable difference in VTEC between 2009 and 2014, with the latter year exhibiting higher VTEC values. The VTEC values for the DF signals in 2014, particularly in the CODG and b5mg datasets, are significantly elevated compared to the SF signals, likely due to the enhanced correction of ionospheric errors in DF measurements.

As shown in Figure 11, the inability to directly correct for ionospheric delay increased positioning errors for SF GPS. The lower VTEC values observed in 2009 reflect reduced ionospheric activity, which may contribute to faster convergence times, as earlier mentioned (Figure 6a), and improved positioning accuracy (Figure 7). This finding is consistent with previous studies that indicate SF users are more susceptible to ionospheric conditions, experiencing degraded accuracy during periods of high VTEC. Research by [30] highlights that SF positioning is prone to greater inaccuracies under high VTEC conditions, with ionospheric models offering limited mitigation in such scenarios, especially for SF users. On the other hand, DF PPP gradually corrects for ionospheric delay with undifferenced and uncombined observations [31, 32], thereby reducing the impact of elevated VTEC on positioning accuracy (Figures 8 and 10). Nevertheless, the higher VTEC levels in 2014 still necessitate adjustments in the PPP process to account for larger ionospheric variations, potentially slowing convergence. However, accuracy remains more stable than in SF PPP.

Our study indicates that during high solar activity (high VTEC) periods, PPP convergence times can extend by 30–40 % due to increased ionospheric noise, confirming that DF receivers perform better under these conditions, maintaining horizontal accuracy within 10–15 mm even when VTEC exceeded 50 TECU. This aligns with the DF VTEC measurements in 2014, which show elevated values but still allow for accurate positioning due to the correction capabilities of DF systems. The analysis further demonstrates that higher TR IONEX files (b5mg) provide more detailed and accurate representations of VTEC, which are essential for correcting ionospheric errors in GNSS applications, particularly during periods of significant ionospheric activity. The

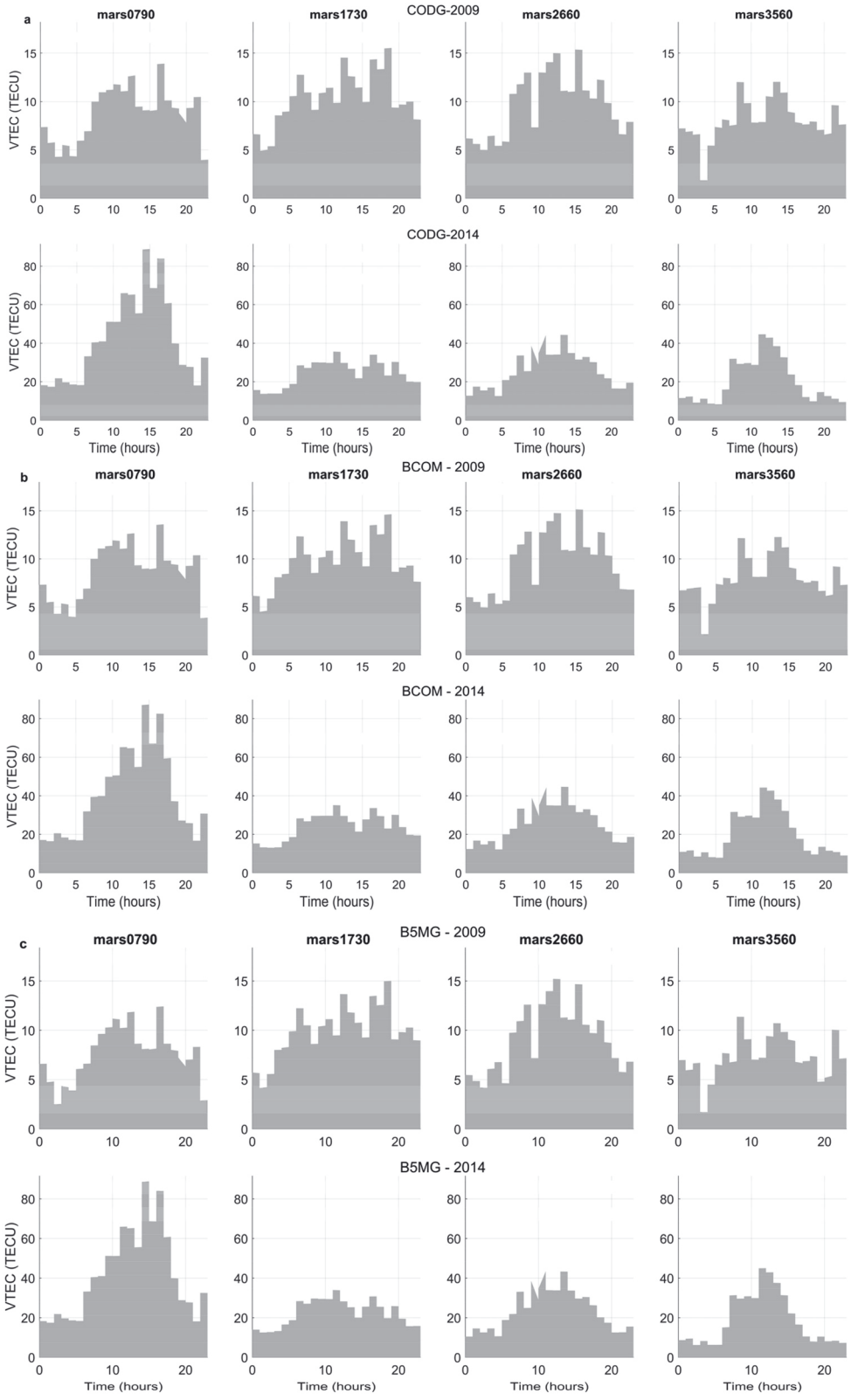

Figure 11: VTEC comparison for three IONEX files at station MARS (Lat: 43.279, Lon: 5.354) in 2009 and 2014: (a) CODG, (b) bcom, and (c) b5mg, using single frequency.

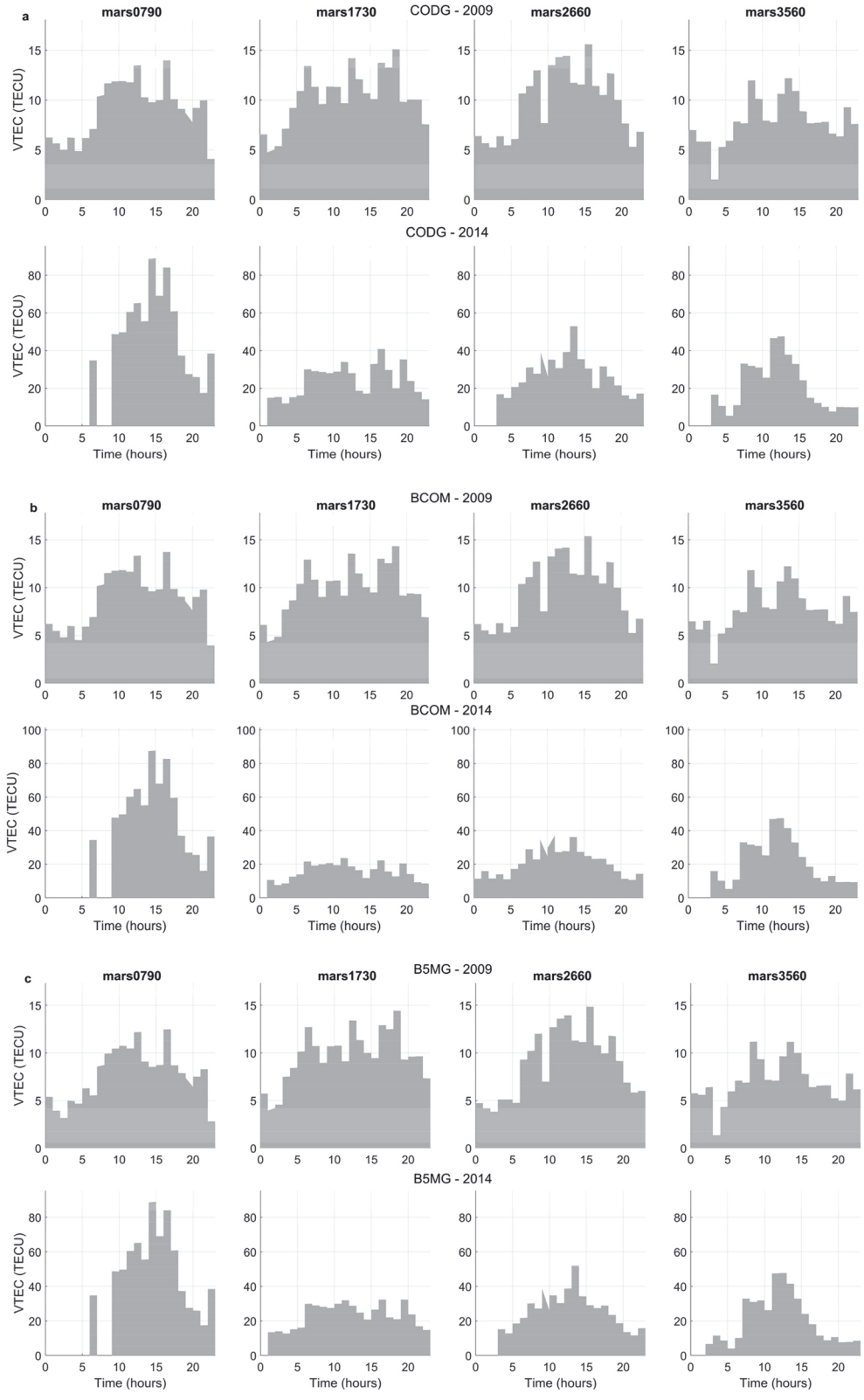

Figure 12: VTEC comparison for three IONEX files at station MARS (Lat: 43.279, Lon: 5.354) in 2009 and 2014: (a) CODG, (b) bcom, and (c) b5mg, using dual frequency.

choice of TR in IONEX files directly affects GNSS positioning accuracy, with higher resolutions offering superior performance but at the cost of increased data processing requirements. For high-precision applications, such as surveying and scientific research, b5mg is advantageous, while bcom might be a suitable compromise for general use.

5 Conclusions

This study systematically analyzed the influence of solar activity and the use of different IONEX files with varying TRs on PPP convergence times and positioning accuracy between 2009 and 2014. VTEC analysis was conducted at the MARS station, reflecting the correlation and impact of various GIMs. The findings underscore the critical role of solar cycles and high-resolution GIMs in improving GNSS performance.

The study highlighted a significant increase in VTEC during 2014, a year closer to the solar maximum, compared to 2009, near the solar minimum. This increase in VTEC directly impacted PPP convergence times, particularly for SF strategy. To elaborate, using DF signals consistently reduced convergence times compared to SF models, especially during high solar activity periods, with the most substantial improvement observed during the March equinox of 2009 using the CODG IONEX file.

TR IONEX files, such as b5mg, significantly enhanced positioning accuracy, particularly for DF users. These findings suggest that higher TRs in GIMs can effectively mitigate ionospheric errors, especially during periods of high solar activity. This study underscores that for high-precision GNSS applications, especially during solar maximum periods, DF systems combined with high-resolution GIMs are essential to achieve optimal convergence times and positioning accuracy.

The study recommends further exploration of higher TR GIMs and their potential to enhance PPP performance under varying ionospheric conditions, it also recommends a deeper investigation into the seasonal effects on GNSS accuracy. Overall, this work provides valuable insights into optimizing PPP by considering both solar activity and the choice of GIM TR, offering practical implications for improving GNSS accuracy and reliability in diverse conditions.

Acknowledgments: The authors are grateful to thank IGS website for providing the data, and the GIMs that used in our study. Furthermore, we are grateful to the GAMP developers for their hard work and amazing contributions.
Research ethics: Not applicable.
Informed consent: Not applicable.
Author contributions: The authors have accepted responsibility for the entire content of this manuscript and approved its submission.
Use of Large Language Models, AI and Machine Learning Tools: None declared.
Conflict of interest: The authors state no conflict of interest.
Research funding: None declared.
Data availability: IGS website for providing the data, and the GIMs that used in our study. http://www.aiub.unibe.ch/download/CODE/, http://igscb.jpl.nasa.gov/ and http://ionosphere.cn.

References

1. Pereira VAS, Monico JFG, Camargo PDO. Detection of solar flare using IGS network stations: case study for September 6, 2017. Rev Bras Geomát 2021;9:103.
2. Aa E, Zhang SR, Erickson PJ, Wang W, Qian L, Cai X, et al. Significant mid- and low-latitude ionospheric disturbances characterized by dynamic EIA, EPBs, and SED variations during the 13–14 March 2022 geomagnetic storm. J Geophys Res: Space Phys 2023;128. https://doi.org/10.1029/2023ja031375.
3. Ryakhovsky IA, Poklad YV, Gavrilov BG, Bekker SZ. Estimation of the ionospheric D-region ionization caused by X-class solar flares based on VLF observations. J Geophys Res: Space Phys 2024;129:1–11.
4. Gumilar I, Mahdiyanto RA, Bramanto B, Kuntjoro W, Abidin HZ. Study of GNSS multi-constellation performance in single point positioning and differential positioning in Indonesia. J Aeronaut Astronaut Aviat 2022;54:195–214.
5. Hoque MM, Jakowski N. Higher order ionospheric effects in precise GNSS positioning. J Geod 2007;81:259–68.
6. Hoque MM, Jakowski N. Mitigation of higher order ionospheric effects on GNSS users in Europe. GPS Solut 2008;12:87–97.
7. Shapkin A. И ГЕОИНУОдМАТИКА Алгорилм оценки абсолюлного Полного элекlронного соДержания ионосферы По Данным Двуlчаслолныl фазовыl и Дальнослныl сПулниковыl измерений. Minsk, Belarus: Informatics; 2024.
8. Xie W, Su H, Wang K, Liu J, Wu M, Zou M, et al. Real-time LEO satellite clock estimation with predicted LEO satellite orbits constrained. GPS Solut 2024;28:172. https://doi.org/10.1007/s10291-024-01723-6.
9. Bos MS, Penna NT, Baker TF, Clarke PJ. Ocean tide loading displacements in western Europe: 2. GPS-observed anelastic dispersion in the asthenosphere. J Geophys Res Solid Earth 2015;120:6540–57.
10. Liu Q, Hernández-Pajares M, Lyu H, Goss A. Influence of temporal resolution on the performance of global ionospheric maps. J Geod 2021;95:34. https://doi.org/10.1007/s00190-021-01483-y.
11. Li F, Zhang Q, Zhang S, Lei J, Li W. Evaluation of spatio-temporal characteristics of different zenith tropospheric delay models in Antarctica. Radio Sci 2020;55:1–16.
12. Sam-Khaniani A, Naeijian R. Evaluation of modified saastamoinen ZTD model using ground-based GPS observation over Iran. Earth Sci Inform 2023;16:2339–53.

13. Lutz S, Schaer S, Meindl M, Dach R, Steigenberger P. Higher-order ionosphere modeling for CODE's next reprocessing activities. Washington, D.C: American Geophysical Union; 2010, 2002:2002 p.
14. Zeng T, Sui L, Xiao G, Ruan R, Jia X. Computationally efficient dual-frequency uncombined precise orbit determination based on IGS clock datum. GPS Solut 2019;23:1—14.
15. Datta-Barua S, Walter T, Blanch J, Enge P. Bounding higher order ionosphere errors for the dual frequency GPS user. In: Proc. inst. navig. — 19th int. tech. meet. satell. div. ION GNSS 2006; 2006, vol 3:1377—92 pp.
16. Wang C, Fan L, Wang Z, Shi C. Assessment of global ionospheric maps over continental areas using precise point positioning technique. J Spat Sci 2020;65:25—39.
17. Jerez GO, Hernández-Pajares M, Prol FS, Alves DBM, Monico JFG. Assessment of global ionospheric maps performance by means of ionosonde data. Remote Sens 2020;12:1—18.
18. Jerez GO, Hernández-Pajares M, Goss A, Prol FS, Alves DBM, Monico JFG, et al. Two-way assessment of ionospheric maps performance over the Brazilian region: global versus regional products. Sp. Weather 2023;21. https://doi.org/10.1029/2022sw003252.
19. Marchenko SV, Deland MT, Lean JL. Solar spectral irradiance variability in cycle 24: observations and models. J Space Weather Space Clim 2016;6:1—19.
20. Kane RP. Some implications using the group sunspot number reconstruction. Sol Phys 2002;205:383—401.
21. You D, Has S. The sun. Cambridge, MA: MIT Press; 2007:68—69 pp.
22. Ren X, Chen J, Li X, Zhang X. Ionospheric total electron content estimation using GNSS carrier phase observations based on zero-difference integer ambiguity: methodology and assessment. IEEE Trans Geosci Remote Sens 2021;59:817—30.
23. Dow JM, Neilan RE, Rizos C. The international GNSS service in a changing landscape of global navigation satellite systems. J Geod 2009;83:191—8.
24. Kouba J. A guide to using international GNSS service (IGS) products. Geod Surv Div Nat Resour 2009;6:34.
25. Shi C, Fan L, Li M, Liu Z, Gu S, Zhong S, et al. An enhanced algorithm to estimate BDS satellite's differential code biases. J Geod 2016;90:161—77.
26. Zhou F, Dong D, Li W, Jiang X, Wickert J, Schuh H. GAMP: an open-source software of multi-GNSS precise point positioning using undifferenced and uncombined observations. GPS Solut 2018;22:1—10.
27. Li M, Zha J, Yuan Y, Liu T, Zhang X, Zhao C. A unified model of multi-GNSS and multi-frequency precise point positioning for the joint estimation of ionospheric TEC and time-varying receiver code bias. J Geod 2024;98:1—14.
28. Wu Q, Zhang P, Sun M, Liu S, Wang H, Chen S. Performance evaluation of GIMs released by different IGS ionosphere associate analysis centers in ionospheric constrained single-frequency precise point positioning. Adv Space Res 2021;68:4834—56.
29. Hernández-Pajares M, Juan JM, Sanz J, Orus R, Garcia-Rigo A, Feltens J, et al. The IGS VTEC maps: a reliable source of ionospheric information since 1998. J Geod 2009;83:263—75.
30. Bidaine B, Lonchay M, Warnant R. Galileo single frequency ionospheric correction: performances in terms of position. GPS Solut 2013;17:63—73.
31. Drewes H, Kuglitsch F, Adám J, Rózsa S. The geodesist's handbook 2016. J Geod 2016;90:907—1205.
32. Platz HD. On the equivalence of ionospheric-free, differenced, and undifferenced, uncombined GNSS network processing. GPS Solut 2023;27:1—10.